Renewable Energy 273 (2026) 126047

Contents lists available at ScienceDirect

Renewable Energy

journal homepage: www.elsevier.com/locate/renene

Short-term renewable energy forecast errors in Europe: Spatial dependence and smoothing potential

Matthias Zech *, Marion Schroedter-Homscheidt, Lueder von Bremen

German Aerospace Center (DLR), Institute of Networked Energy Systems, Carl-von-Ossietzky-Straße 15, Oldenburg, 26129, Germany

ARTICLE INFO

Keywords:
Spatial dependence
Renewable energy forecast errors
Forecast error smoothing
Renewable energy integration

ABSTRACT

Renewable energy forecast errors result in costly countermeasures, including countertrading, redispatch, and increased operating reserves. Correlated regional forecast errors increase risks in renewable energy portfolios, yet their spatial dependencies are poorly understood. Therefore, we derive site-specific correlation lengths and assess the potential for spatial smoothing of forecast errors across Europe from intraday to two-day-ahead. By increasing site separation beyond 150 km, weather-driven renewable energy forecast errors effectively become uncorrelated, reducing mean absolute errors and extreme forecast error events by over 33% for wind energy and approximately 25% for solar energy at day-ahead lead times. Additionally, accounting for principal error directions can reduce the necessary site separation for effective error mitigation. Finally, we evaluate current and planned renewable energy sites in Europe based on these findings and identify regions with elevated forecast errors. This study provides a characterization of renewable energy forecast errors in Europe and offers actionable insights for decision-makers designing resilient renewable energy portfolios.

1. Introduction

With the rapid uptake of renewable energy capacity, accurate renewable energy forecasts are crucial for maintaining a reliable energy system. They support improved bidding strategies in energy markets, enhance operational reliability in transmission, and estimate necessary storage sizes in energy systems [3]. Forecast quality has continuously improved in recent years [1]. At short time scales, new measurement technologies have been introduced, including all-sky cameras [4,5] and satellite imagery [6] for solar energy, along with lidars for wind energy [7,8]. At longer lead times, Numerical Weather Prediction (NWP) models excel in weather forecasting, and renewable energy forecasts have benefited from the advances in NWP modeling, which has improved by approximately one day per decade [9]. With ongoing developments of AI-based weather forecasts [10], further enhancements can be expected.[1]

Despite the improvements, renewable energy forecast errors (**FEs**) will persist due to the chaotic nature of the atmosphere, leading to costly measures such as counter-trading, penalty settlements, redispatch, and curtailment. The costs of FEs are challenging to estimate as they vary on the decision-making problem, yet they are substantial. Studies report median costs due to PV forecast errors ranging from 0.36 to 22.94 USD/MWh [11], with higher PV penetration levels leading to increased costs. Therefore, effective hedging strategies against FEs are essential to reduce both individual and societal costs given these substantial cost contributions.

Increasing the distance between renewable energy sites within a portfolio is known to reduce renewable energy intermittency, as demonstrated for solar energy in Perez et al. [12] and for wind energy by St. Martin et al. [13]. Similar spatial smoothing effects have also been reported for FEs. In Italy, solar energy forecast errors (**SE-FEs**) are 34% lower at the national level than at individual market zone [14]. In Germany, Lorenz et al. [15] showed that SE-FEs can be reduced from 0.10–0.12 Wh/Wp for single sites to 0.06–0.09 Wh/Wp in regions of 200 by 120 km. Furthermore, the decrease in cross-correlation with increasing site distances can be modeled for SE-FEs using the same hyperbolic functions proposed for PV generation data, as shown in Perez et al. [16]. Like solar energy, wind energy forecast errors (**WE-FEs**) can also be significantly smoothed through spatial aggregation. Saleck and Von Bremen [17] found that forecast accuracy improves when considering multiple wind turbines within a wind farm, with aggregated forecasts outperforming those for individual turbines in Germany. Focken et al. [18] observed a sharp decline in cross-correlation for simulated WE-FEs in Germany, with correlation values below 0.2 within 100 km of site separation at a 12-hour lead time. Their findings indicate that cross-correlation increases with longer lead times, while WE-FEs become nearly uncorrelated at site separations

* Corresponding author.
E-mail address: matthias.zech@dlr.de (M. Zech).

[1] For a comprehensive review of advancements in renewable energy forecasting, please refer to Sweeney et al. [1],Paletta et al. [2].

https://doi.org/10.1016/j.renene.2026.126047
Received 10 December 2025; Received in revised form 5 June 2026; Accepted 6 June 2026
Available online 13 June 2026

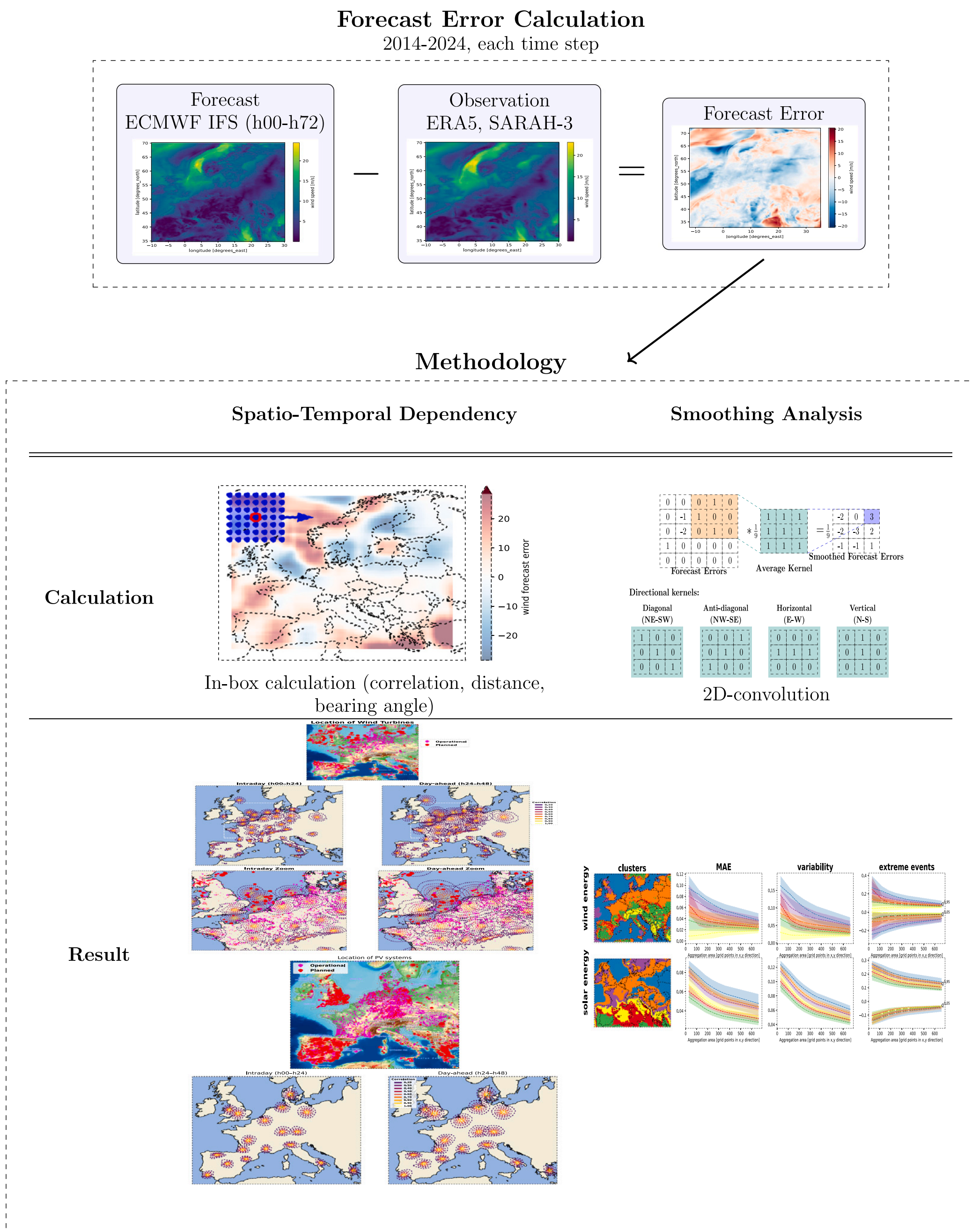

Fig. 1. Overview of the methodology of this study for the derivation of forecast error maps and its analysis of spatio-temporal dependency and smoothing potential. For the smoothing analysis, the illustrated kernels are 3 by 3 for clarity, but are actually adapted to all used aggregation levels.

beyond 500 km. This pattern is consistent with results from Denmark, where day-ahead WE-FEs become uncorrelated at approximately 500 km distances [19]. Studying larger spatial domains promises to identify local particularities, such as those in Europe noted in Hüsch et al. [20], where wind speed NWP forecast errors indicate that regions in complex terrain (e.g., Alps) exhibit much smaller spatial dependence of forecast errors than regions in flat terrain.

While these studies analyze the smoothing effect of renewable energy FEs in selected regions, a comprehensive pan-European investigation of the spatial dependence of renewable energy FEs and their smoothing potential is still lacking. This relates to site-specific characteristics, potential smoothing effects, and directional dependence in FEs. This study addresses this gap by systematically examining renewable energy FEs, focusing on intraday, day-ahead, and two-days-ahead WE-FEs and SE-FEs. We investigate intersite correlations of renewable energy FEs by deriving site-specific correlation lengths, exploring aggregation effects, and analyzing directional dependence. By applying clustering techniques, we identify regions with similar behaviors regarding correlation decay and the smoothing effect. The results are crucial for understanding the spatial dependence of renewable energy FEs. This knowledge is important for energy policy decision-makers to design better portfolios and for industrial stakeholders, such as distribution grid operators and renewable energy portfolio managers, who often face large-scale forecast errors associated with significant societal costs (redispatch, counter-trading).

The paper is structured as follows: Section 2 details the datasets and methodology. Section 3 presents the analysis results, including spatial dependence characterized by correlation lengths and clustered regions with similar correlation decay. We then examine the effect on the aggregated time series, derive directional dependence, and investigate

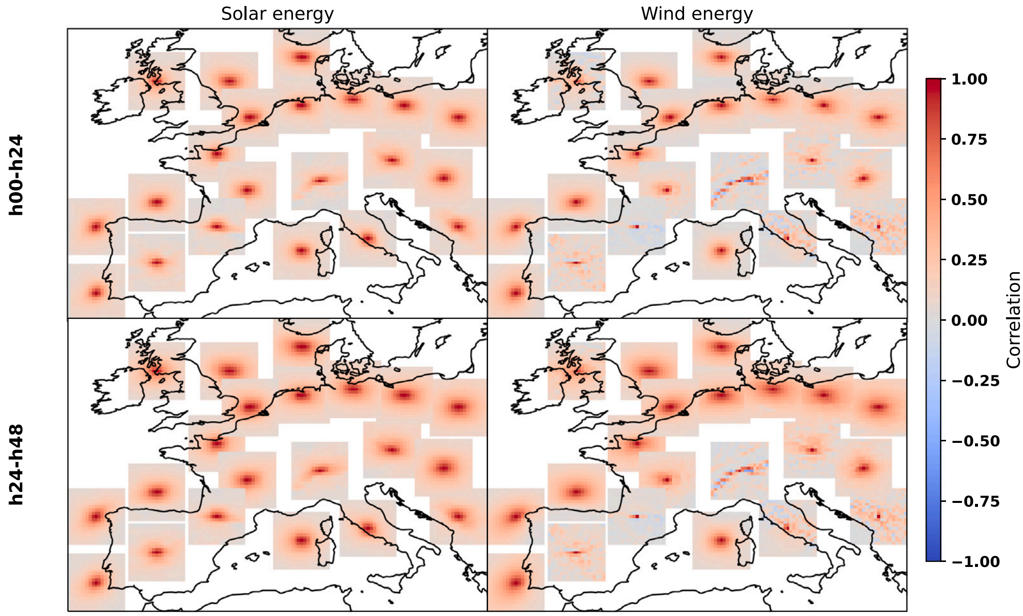

Fig. 2. Illustration of the correlation maps at selected points and changing lead times. For illustration, the bounding box is only a one fourth of the actual bounding box.

the impact on the current and planned European renewable energy portfolio. Finally, we discuss our findings and their implications for future research.

2. Data and methods

The data and methodology of this study are shown in Fig. 1.

2.1. Data

The renewable energy forecasts are derived from the ECMWF IFS model, a widely used NWP model in renewable energy forecasting [1]. We focus on lead times of up to two days ahead (h00-h24, h24-h48, h48-h72) that overlap with key energy decision-making processes, such as intraday and day-ahead trading and the generation of two day-ahead congestion forecasts [21]. We derive FE maps using ERA5 reanalysis data [22]. For solar radiation (direct and diffuse horizontal), we utilize ERA5 and satellite data from SARAH-3 [23], as irradiance from satellites is more accurate than from reanalysis data [24]. The SARAH-3 irradiance maps are converted into solar radiation using the aggregation technique proposed in Zech et al. [25], which accounts for site-specific satellite scan times. To match the spatial resolution of forecasts and reanalysis, we spatially averaged the SARAH-3 data to the ERA5 grid resolution (0.25°). We analyzed a 10-year period (2014–2024) focusing on energy-relevant parameters for solar energy (global and direct radiation, near-surface temperature) and wind energy (wind speed at 100 m, surface roughness). To study the effect on renewable energy, meteorological parameters are converted into maximum retrievable energy (capacity factors) using the `atlite` [26] library. Calculating capacity factors provides spatially comparable potentials that can be converted into energy equivalents by multiplying with the installed capacity. Capacity factors are derived from a characteristic onshore wind turbine (Vestas V112, 3 MW), an offshore wind turbine (NREL reference turbine, 5 MW), and a PV panel (south-oriented crystalline silicon panel, 30° tilt angle), inspired by the widely used `pypsa-eur` energy system model [27]. This approach results in solar and wind energy capacity factors at the same resolution as the NWP model (approximately 30 km). Solar radiation values with solar elevation angles below 10 degrees are excluded from the analysis to eliminate sunrise and sunset situations, which are known to have larger FEs, and to remove all nighttime values. For correlation calculations, the FE time series were normalized by deriving the hour-of-the-year minimum and maximum values from the 10-year period to eliminate the climatological and diurnal signals.

To enhance the generalizability of our findings, we also derived bidding zone level FE time series from ENTSO-E. These time series are derived from day-ahead forecasts and actual solar and wind energy generation data. We removed unreliable time series (consistent biases) through visual inspection and normalized them using a 60-day running mean and standard deviation for each hour of the day. This eliminates seasonality and avoids assumptions about varying generation capacities in the bidding zones.

2.2. Spatial dependence between forecast errors

2.2.1. In-box correlation-distance relationships

To estimate the spatial dependence of the FEs, we derive correlation-distance relationships between sites, quantifying how correlation between FEs decays with increasing site separation. Specifically, for each site s, we consider its correlation $\rho_{s,s'}$ with neighboring sites s', their separation distances $d_{s,s'}$, and their bearing angles $\theta_{s,s'}$, which is used to assess directional influence. For gridded datasets derived from NWP outputs, calculating $\rho_{s,s'}$, $d_{s,s'}$ and $\theta_{s,s'}$ between every pair of grid points quickly exceeds computational limits.[2] To reduce computational time, we consider only site pairs within a box of 18 by 18 grid points, which are approximately 500 km (Fig. 1). This approach is valid, as all calculated correlations in this study decay to near-zero values within the specified box size, and long-distance correlations for forecast errors were not observed. This approach leads to correlation maps within the bounding box, as illustrated in Fig. 2.

Furthermore, correlation-distance pairs ($\rho_{s,s'}$ and $d_{s,s'}$) are obtained for each grid point and used to derive site-specific correlation lengths $\xi_s(r_n)$. Following the non-parametric formulation from St. Martin et al.

[2] Specifically, calculating correlations, distances, and bearing angles for one site with respect to all others requires $3n(n-1)$ calculations, where n is the number of grid points. For a moderately sized grid of $100 \times 100 = 10^4$ grid points, this leads to around $\times 10^8$ calculations.

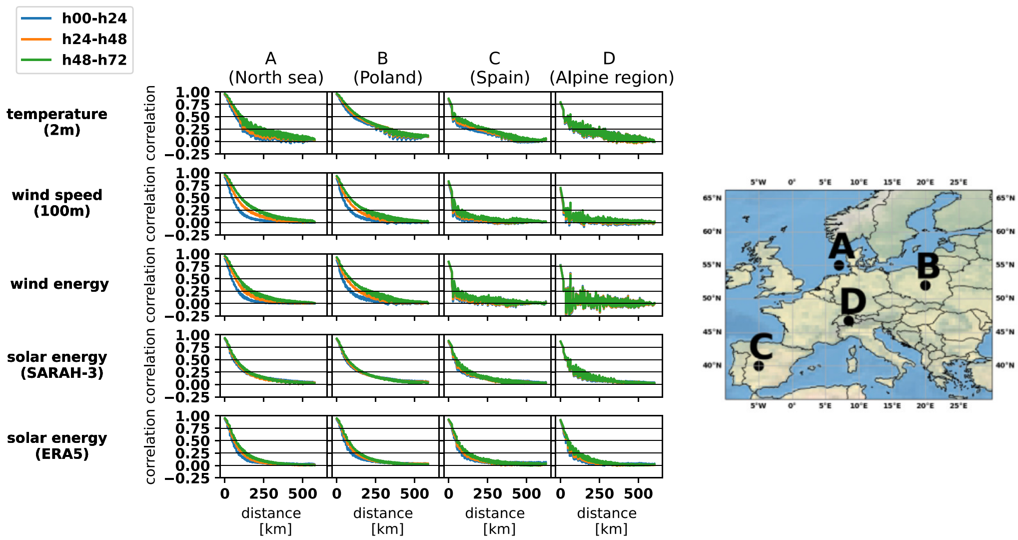

Fig. 3. Correlation-distance curves for four selected sites and the three considered lead times, the sites are selected to be as diverse as possible. All correlation curves decay to zero representing reasonable box sizes.

[13], we calculate correlation lengths by numerical integration of the correlation over distance using the trapezoidal rule:

$$\xi_s(r_n) = \sum_{k=1}^{n} \frac{1}{2}(r_k - r_{k-1})(\rho_{rk} + \rho_{rk-1}) \qquad \forall s. \tag{1}$$

2.2.2. Directional dependence

The bearing angles $\theta_{s,s'}$ describe the direction between pairs of grid points. To relate these directions to the correlation pairs $\rho_{s,s'}$, each pair $(\rho_{s,s'}, \theta_{s,s'})$ is converted into Cartesian vector components as

$$u_{s,s'} \;=\; \rho_{s,s'} \cos\!\left(\theta_{s,s'} \times \tfrac{\pi}{180}\right), \tag{2}$$

$$v_{s,s'} \;=\; \rho_{s,s'} \sin\!\left(\theta_{s,s'} \times \tfrac{\pi}{180}\right). \tag{3}$$

Each vector has length $\rho_{s,s'}$ and points in the direction $\theta_{s,s'}$. Using average vectors for plotting is invalid, as leading directions may influence each other and potentially cancel out (e.g., in case of strong North and South orientations). We utilize angle bins of 15° to gather the two most prominent directional modes

$$\left(u_s^{(1)}, v_s^{(1)}\right) \quad \text{and} \quad \left(u_s^{(2)}, v_s^{(2)}\right),$$

whose magnitudes represent the strongest directional modes in $\{\rho_{s,s'}\}$.

2.3. Spatial accumulation of forecast errors

Correlation is scale invariant and therefore does not account for the magnitude of the FEs. However, FE magnitudes are essential, because they characterize the expected error within a spatial domain. To quantify the spatial smoothing potential, we derive spatially accumulated FE time series for various aggregation areas (84, 140, 196, 252, 308, 588, 868, 1428 km). The aggregation is implemented using a spatial convolution with kernels of different sizes on the grid, as illustrated in Fig. 1. Furthermore, we analyze the impact of the smoothing direction, determining whether larger FE smoothing can be achieved in specific directions. We construct a 140 by 140 km kernel for four directions: diagonal (north-west to south-east), antidiagonal (north-east to south-west), horizontal (west to east), and vertical (north to south). Since the NWP model data and observations are not equidistant, they are converted to the Lambert Azimuthal Equal-Area projection before aggregation to ensure comparable spatial areas.[3]

The impact of aggregation is measured by three metrics: the Mean Absolute Error ($\frac{1}{T}\sum_t^T |\epsilon_{t,s}|$), the standard deviation of the forecast errors ($\sigma_t(\epsilon_{t,s})$), which characterizes the variability of the FE distribution, and the 5th and 95th percentiles, which capture extreme positive and negative FE events.

2.4. Clustering sites with similar spatial behavior

The correlation–distance relationships and aggregated FE statistics time series are calculated for each grid point, resulting in a large number of difficult-to-summarize, multi-dimensional data for each grid point. To facilitate the data interpretation, we apply k-means clustering [28] to the site-specific data. More specifically, each site is assigned to a cluster based on its characteristics, which is then used to make grouped visualizations and comparisons between sites with similar spatial-dependence or smoothing potential. The k-means algorithm is repeated for different numbers of clusters, ranging from 2 to 8. The final number of clusters is determined through visual inspection, based on the ability to distinguish meaningful spatial patterns while retaining interpretability. Clustering is applied twice in this study: first to the correlation-distance pairs, and second to investigate the smoothing effect derived from the spatially aggregated FE time series.

3. Results

3.1. Spatial correlation between forecast errors

Fig. 3 illustrates the correlation–distance relationships for four selected points regarding temperature, global horizontal irradiance, wind speed, wind energy, and solar energy across the three analyzed lead times. The four sites were chosen for their diversity: coastal (A), continental Eastern Europe (B), lower latitudes (C), and complex terrain (D). In all cases, correlations decay to near zero within the distance range (< 500 km), indicating that significant correlation does not persist beyond this limit, and the box size for the correlation calculation is appropriately chosen. Within the first 250 km, correlations drop below 0.1 for all considered parameters. Temperature shows the slowest decay, particularly in the site in Poland, where the correlation drop within the first 250 km is less pronounced than for other parameters, indicating anomalous correlation behavior.

Fig. 4 shows the correlation-distance relationships for all sites for SE-FEs and WE-FEs. Each site is assigned to a cluster identifiable by different colors. This results in two clusters for solar energy and four

[3] Note that the original ECMWF IFS model is calculated on an octahedral reduced Gaussian grid with relatively constant grid point distances.

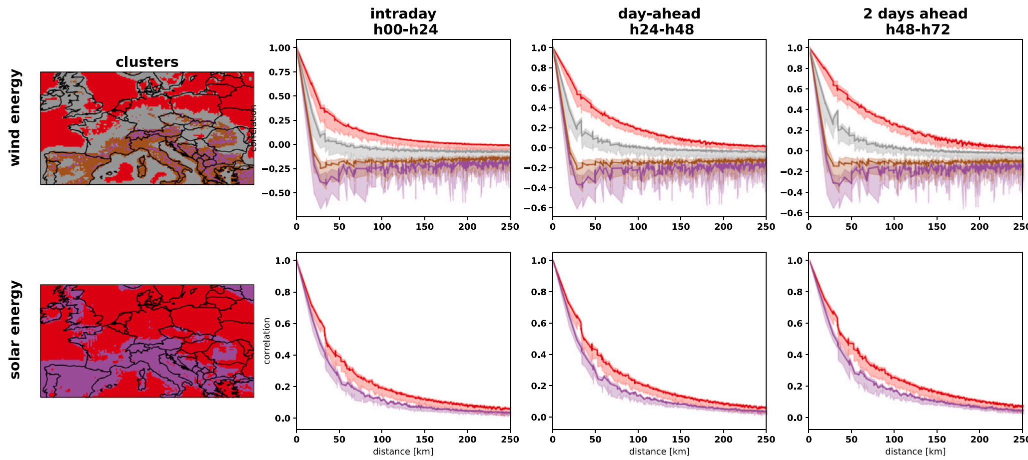

Fig. 4. Clustered correlation-distance relationships of renewable energy FEs. The color on the left maps indicate the belonging of one site to its respective cluster, and the other plots the values of the respective cluster for the different lead times (the line represents the mean, the shaded bands the 5th and 95th percentile). The clustering leads to four diverse wind energy groups and two similar solar energy groups.

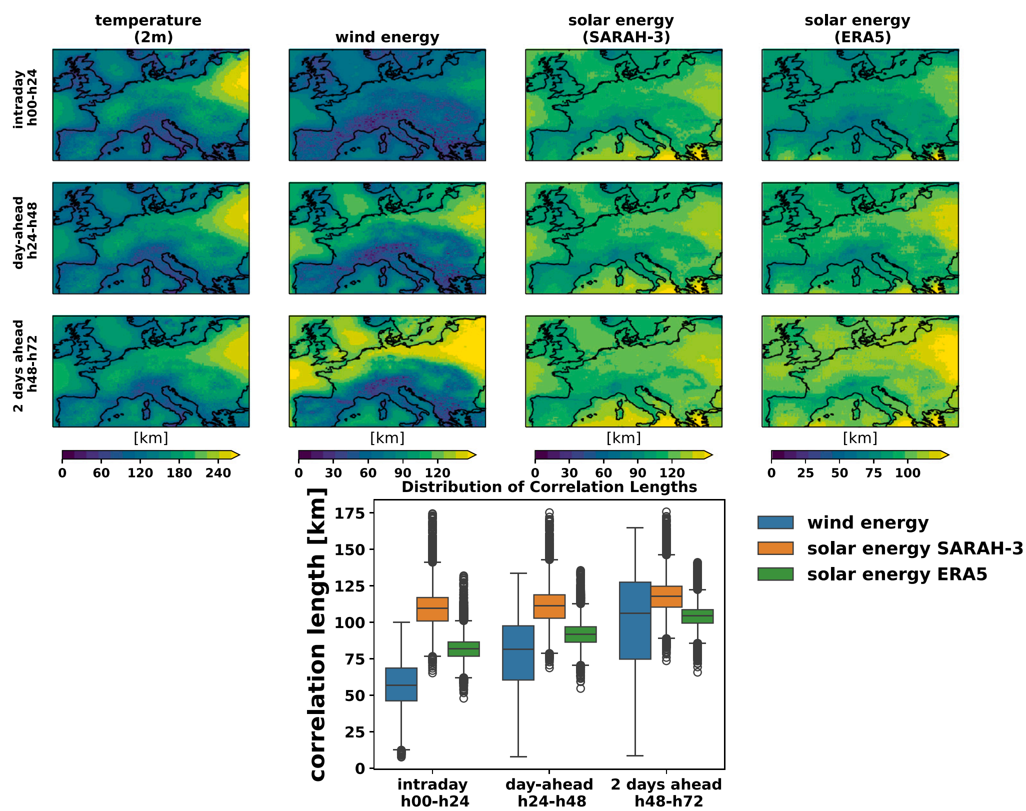

Fig. 5. Correlation lengths of the renewable energy FEs derived from the trapezoidal rule. The boxplot indicates the range of correlation lengths for all sites subject to different lead times. For validation and robustness, two different solar radiation datasets (ERA5, SARAH-3) are used.

for wind energy. *WE-FEs* have large differences between the different clusters and thus spatially different distance-correlation relationships. In the red cluster, correlation decays slowly with increasing distances, dropping below 0.25 between 50 and 100 km across all lead times. Geographically, this cluster includes sea surfaces and coastal regions of France, Germany, and Eastern Europe, areas known for high wind speeds and substantial onshore and offshore energy capacities. The gray cluster describes sites in Continental Europe, the United Kingdom, and the Mediterranean. Compared to the red cluster, the gray cluster shows weaker spatial dependence in the first 50 km, though still noticeably stronger than the purple and brown clusters. The brown and purple clusters denote areas with significant orographic changes (Alps, Pyrenees, Apennines, Balkan Mountains, Caucasus Mountains), exhibiting steep correlation drops over short distances (below 50 km), resulting in anticorrelations at very short distances (up to −0.5). Anticorrelation indicates strong smoothing potential, as nearby sites with underestimation (or overestimation) are more likely to have overestimated (or underestimated) WE-FEs. Longer lead times suggest stronger spatial dependence, with the red cluster exhibiting the greatest sensitivity to lead time, while other clusters demonstrate either smaller (gray) or no clear lead time sensitivity (purple and brown). Northern Europe exhibits larger forecast errors with longer lead times compared to regions in complex terrain or Southern Europe.

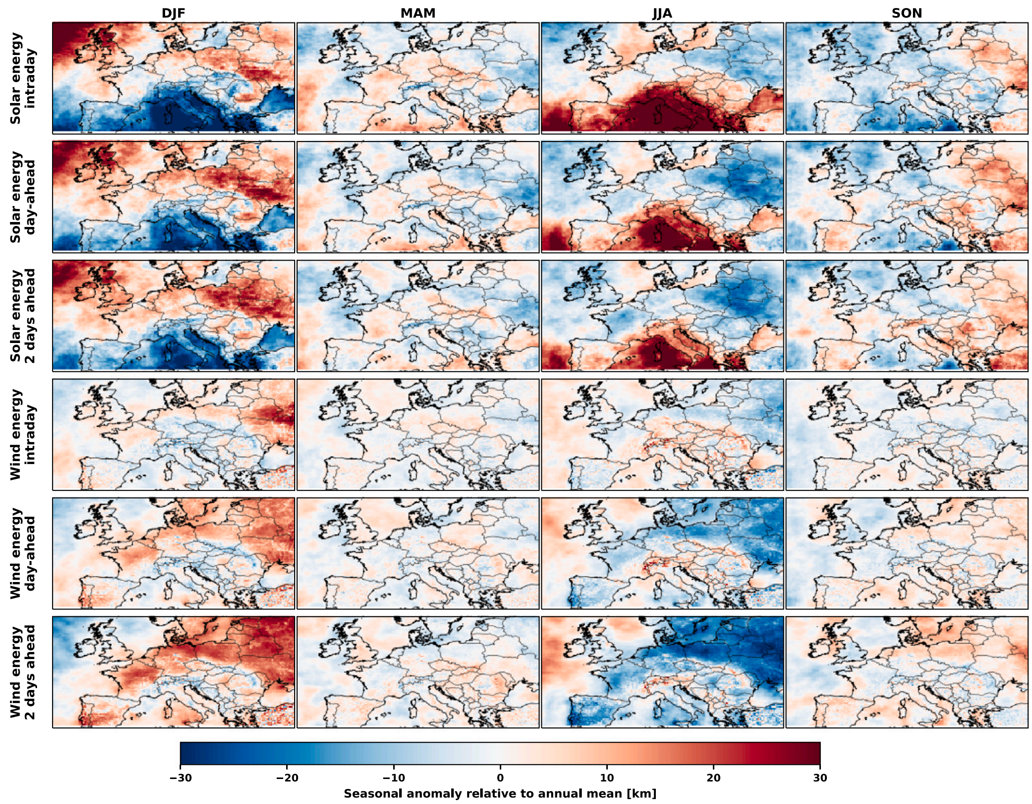

Fig. 6. Seasonal variation in correlation lengths for wind and solar energy for different lead times (2014–2024) with large differences between wind and solar.

For *SE-FEs*, two distinct clusters are selected with spatial dependence patterns, while the differences between the clusters are much smaller compared to WE-FEs. The purple cluster encompasses Southern Europe (Iberian Peninsula, Italy, and Southern France) and exhibits lower spatial dependence between FEs, while the red cluster represents the remaining regions in Europe with slightly higher spatial dependence. Similar to wind energy, SE-FEs sharply decline in the first 150 km (correlation below 0.2). Furthermore, both clusters show sensitivity to longer lead times which can be more accurately quantified by investigating correlation lengths.

Correlation lengths indicate the distance at which a site becomes uncorrelated with neighboring sites, as shown in Fig. 5. Consistent with previous findings, higher latitudes result in greater spatial dependence in WE-FEs compared to lower latitudes, particularly in Northern Europe and the European Plain. WE-FEs correlation lengths rise sharply, with median lengths increasing from 50 km at intraday lead time to about 100 km at a two-days-ahead lead time. SE-FEs show larger correlation lengths at short lead times of around 75 km for ERA5 (110 km for SARAH-3), however, the increase with longer lead times is relatively small compared to WE-FEs. Across the considered forecast ranges, median correlation lengths for WE-FEs increase by approximately 25 km per additional day of forecast lead time, while for SE-FEs increase by about 10 km. Due to the steep increase in correlation lengths of WE-FEs in the European Plain and the modest increase of SE-FEs, WE-FEs have correlation lengths at one-day lead time similar to SE-FEs and exceed them at two-day lead time.

Interestingly, SE-FEs validated on satellite-derived radiation (SARAH-3) show correlation lengths greater than those derived from reanalysis. This may seem counterintuitive, as satellite-derived irradiance displays greater variability due to higher spatial resolutions (0.25° in ERA5 vs. 0.05° in SARAH-3), however, ERA5 is based on the ECMWF IFS model (cycle CY41R2) and shares much closer model physics with the ECMWF HRES forecast than the semi-empirical models to derive irradiance from satellites.

The aforementioned statistics represent 10-year averages and therefore do not capture seasonal differences in spatial dependence. To address this, Fig. 6 shows seasonal deviations from full-year correlation lengths. During winter months (DJF), WE-FE correlation lengths, and to a lesser extent, SE-FEs increase in the European Plain, reaching anomalies of about 30 km in correlation length at a two-day-ahead lead time. In summer months (JJA), this pattern reverses, with correlation length decreases of about 30 km compared to the average. This can be explained by the prominent drivers of the weather in the mid-latitudes. In the winter months, weather typically exhibits synoptic-scale dynamics, such as a stronger jet stream, active frontal systems, and enhanced baroclinicity, which lead to significant error growth. In contrast, summer weather is more strongly influenced by surface heating and convection, resulting in localized error patterns. This explains why the correlation lengths of WE-FEs are smaller in the summer months and larger in the winter months, with the European Plain more affected than Southern Europe. SE-FEs show a different seasonal pattern. While they show a similar pattern in the European Plain for summer and winter, although with a much smaller magnitude, Southern Europe deviates from this pattern with larger correlation lengths in summer than in winter. As these tend to increase with longer lead times and are thus more influenced by initial state estimation, plausible reasons include erroneous clear-sky model assumptions between satellite-derived irradiance and ECMWF forecasts.

To increase the robustness of the correlation analysis, we extend to day-ahead forecast errors for European bidding zones retrieved from ENTSO-E, representing regional best estimates of actual and forecasted feed-ins of the European renewable energy portfolio. Fig. 7 displays the correlations between these day-ahead FEs, with and without normalization, to assess the significance of correcting for daytime and seasonal variation. When normalized, correlations between the bidding zones are weak, reflecting isolated relationships between neighboring zones, except for closely linked zones like DK1 and DK2 (SE-FEs: 0.37; WE-FEs: 0.30) and among Italian bidding zones. In contrast, without normalization, notably stronger correlations and even anti-correlations emerge for long-range SE-FE relationships. As these patterns only exist for unnormalized FEs, they are likely driven by common diurnal and seasonal

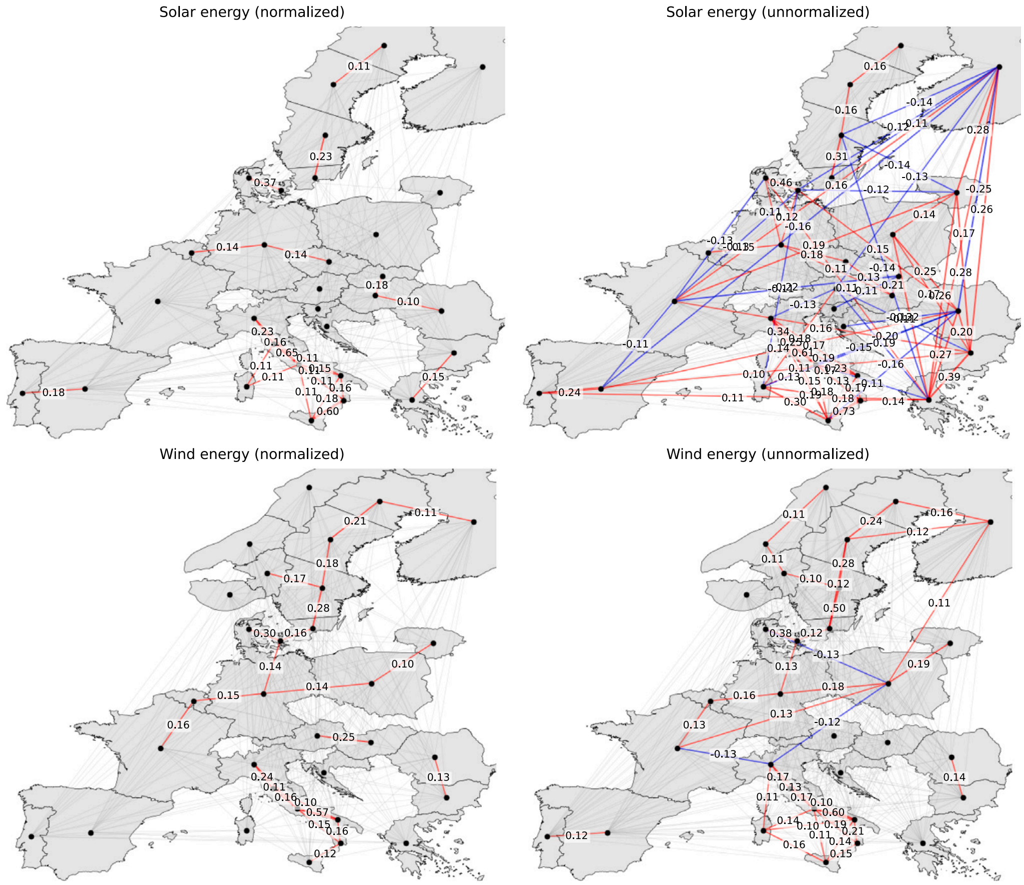

Fig. 7. Correlation between day-ahead forecast errors of the bidding zones, retrieved from ENTSO-E (2015 to 2025). Only correlations above |0.1| are plotted, pairs with no common time series of at least three years are omitted.

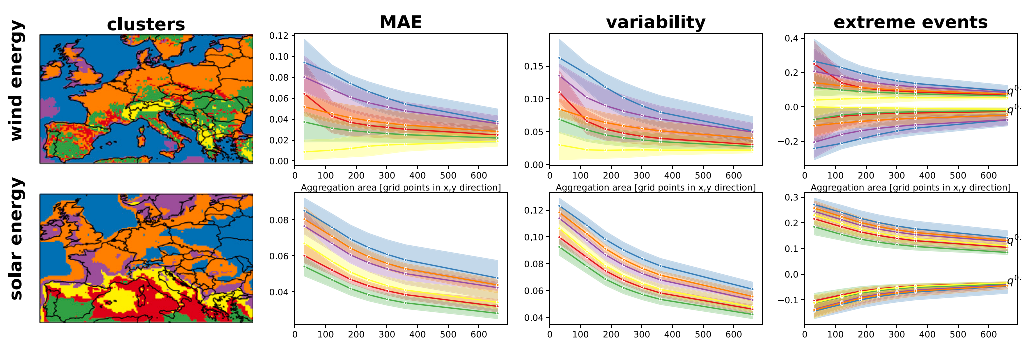

Fig. 8. Day-Ahead smoothing effect of renewable energy forecast errors: Relationship between day-ahead (h24-h48) aggregated forecast errors statistics with larger aggregation distances. The clusters are derived by applying the k-Means algorithm to all variability-distance relationships of each site. Extreme events refer to the 5th and 95th percentiles.

structures rather than from physically meaningful spatial coherence in the SE-FEs. Possible sources include solar geometry, increased error sensitivity at low solar elevation angles [14], inaccuracies in the energy conversion process, and other seasonal error components.

Both data sources (derived grid point level and bidding zone level) indicate that long-range correlations from weather dynamics are unlikely. Weather-related FEs decline sharply within the first 150 km, exhibiting regional and seasonal differences.

3.2. Aggregation of renewable energy forecast errors

As correlation is scale-invariant, it cannot capture the smoothing potential of FEs through spatial separation. Therefore, we derive three metrics from the aggregated FEs as shown in Fig. 8. Similar to the correlation analysis, we use cluster analysis to identify similar regions, focusing on day-ahead FEs due to their significance in day-ahead energy markets.

WE-FEs are divided into six clusters: From highest to lowest criticality (MAE, variability, and extreme events), the blue cluster characterizes sea surfaces, orange represents the European Plain, red and green denote complex terrain regions (e.g., southern Spain, southern France, southern Germany, and eastern Europe), and yellow indicates high-altitude mountain ranges (Alps, Apennines, and the Balkan Mountains). Wind speeds over sea surfaces are greater than in the mountains, resulting in higher WE-FE magnitudes. The magnitude of WE-FEs can be approximately halved among all clusters when considering a region of 500 by 500 km, while an area of 200 by 200 km shows a drop of around a third for the respective metrics. Regions depicted in red (primarily

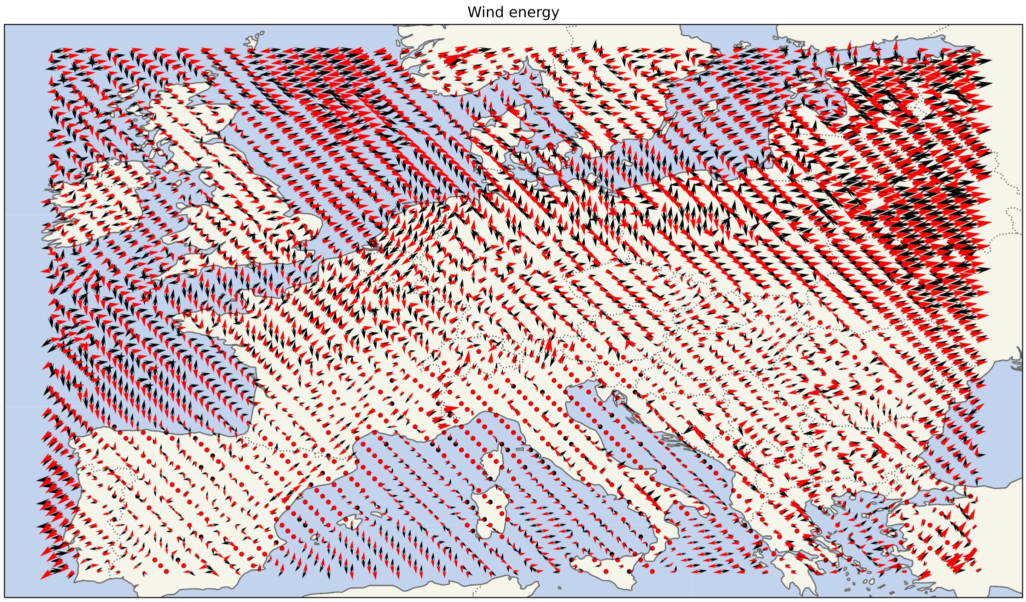

Fig. 9. The two principal directions of wind energy forecast errors. For better visibility, only every fourth vector is plotted. The red arrow indicates the first principal direction, the black arrow the second.

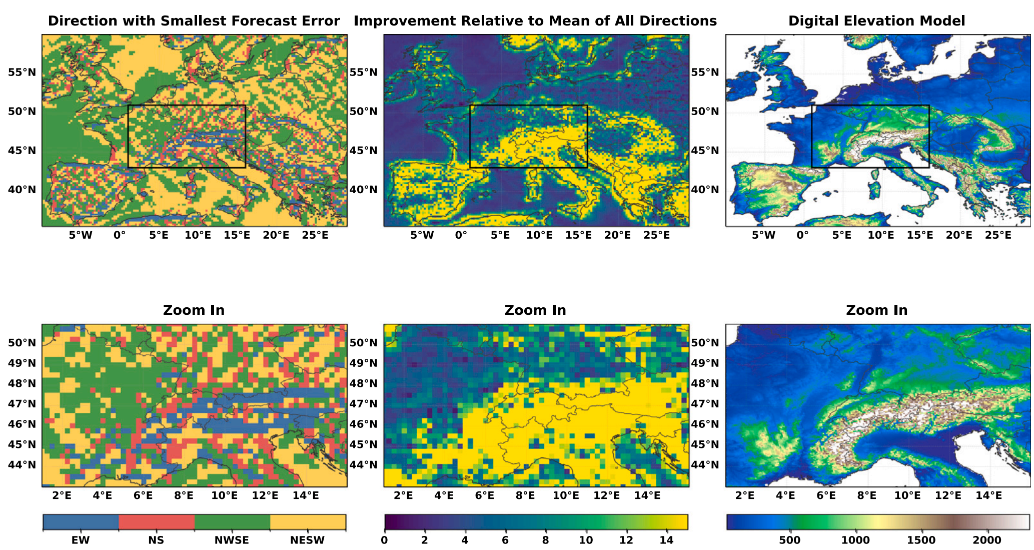

Fig. 10. Benefit of directional smoothing. The lower row presents a zoomed-in into Central Europe for better visibility including an elevation map to understand the relationship of directional smoothing and changing elevations.

located in southern France and northern Spain) exhibit an even stronger decay of these metrics for an area of 150 by 150 km. The orange cluster characterizing the European Plain, previously identified to have strong spatial dependence, shows a smaller but significant smoothing effect for all respective metrics.

SE-FEs clusters are smoother than WE-FEs: The smallest aggregated FEs are found in the southern Iberian Peninsula, followed by the northern Iberian Peninsula, much of Italy, and southern France (yellow). The next cluster describes significant portions of France and Germany (purple, orange), while the cluster with the largest FE statistics is located in eastern Europe and southern Germany (blue). Similar to WE-FE, SE-FEs can be significantly smoothed within each cluster over the first 300 km, i.e. the MAE can often be reduced by around a third for an area of 500 by 500 km (e.g. for the blue cluster from more than 0.08 to less than 0.055). Similar trends are observed for variability and extreme events, indicating an even slightly stronger decay. Interestingly, the curves of the SE-FE clusters are nearly parallel, unlike those of the WE-FEs, suggesting that for SE-FEs, the initial magnitude of the FEs largely determines the aggregation statistics.

3.3. Directional influence

The direction of the FEs has been ignored in the analysis above. If predominant FE directions (e.g., main wind direction or common cloud movements) exist, arranging sites orthogonally to these directions could achieve significant smoothing effects. Therefore, we first derive the principal directions of FEs and then calculate the value of leveraging different directions, as calculated for five pixels (approximately 140 km) relative to the MAE averaged across all directions.

The two principal *WE-FEs* vectors are shown in Fig. 9. The main direction of WE-FEs is eastward, aligning with the westerlies that

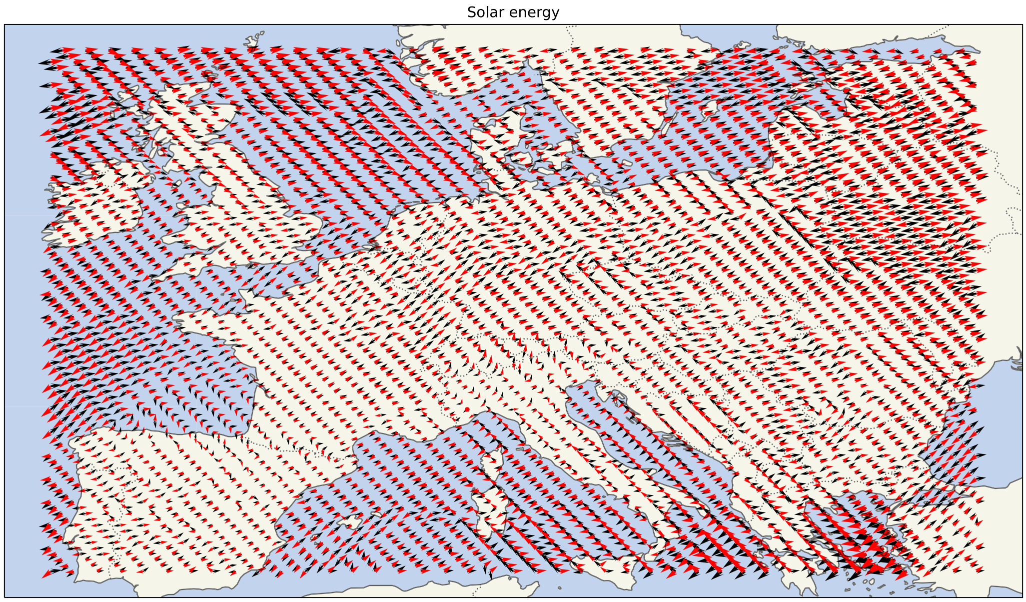

Fig. 11. The two principal directions of solar energy forecast errors (identical to Fig. 9, but for solar energy forecast errors). The patterns are much more uniform for solar energy and westerly influences are noticeable.

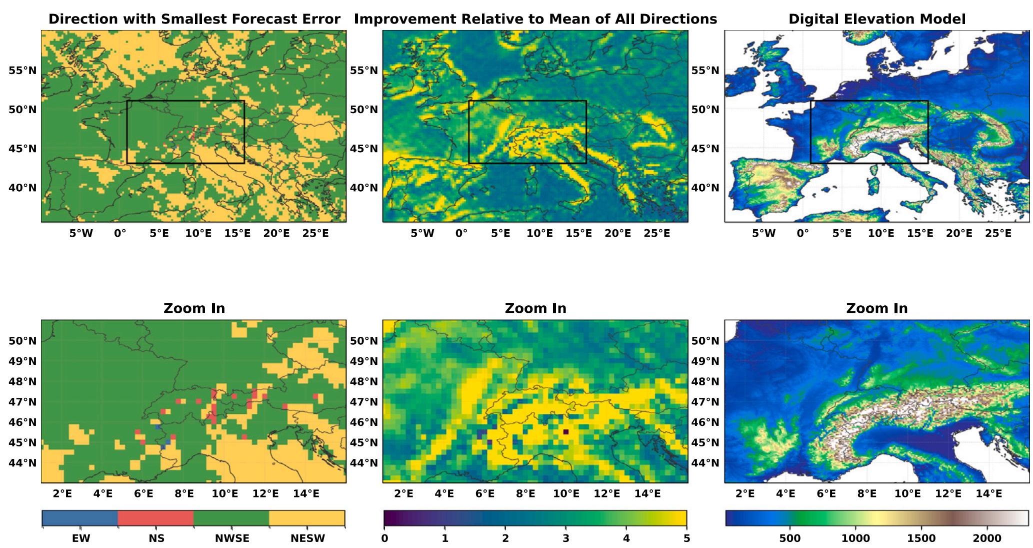

Fig. 12. Benefit of directional smoothing (Identical to Fig. 10, but for solar energy forecast errors). Solar energy only shows advantages regions with strong orographic changes, the benefit is smaller compared to wind energy.

dominate mid-latitude weather in the Northern Hemisphere [29].[4] This is observable over land surfaces in central Europe, eastern Europe, and in the North Sea distant from the coast. At the shore, the predominant WE-FE directions are often different between land and sea surfaces, indicating misalignment in the transition from sea to land surfaces. Principal directions can be leveraged, as shown for different WE-FE directions in Fig. 10 (North-East to South-West, North to South, and North-West to South-East). The regions with the largest benefit are located in complex terrain (Alps, Massif Central, Pyrenees, Apennines), with smoothing improvements exceeding 15%. Near the shore, similar directional smoothing advantages can be observed, such as exploiting the NW-SE orientation in the English Channel and the Northern Sea. Using the NW-SE direction is also promising along land surfaces in northern France's Atlantic coast, a region with substantial onshore wind capacities. Another key area with significant directional smoothing benefits and large onshore wind capacities is Northern Germany, where the NE-SW orientation along land surfaces offer smoothing advantages of approximately 15%.

Compared to WE-FEs, *SE-FEs* have less potential for directional smoothing, though values around 5% remain noticeable. Again, the strong influence of the westerlies is evident, leading to the eastward orientation of SE-FEs (Fig. 11). The impact of the westerlies is particularly noticeable in France, Germany, the United Kingdom, and Eastern Europe. Certain regions deviate from this pattern, such as the Iberian Peninsula, where significant areas point westward and even northward. Like WE-FEs, SE-FEs can utilize directional influences for additional spatial smoothing (Fig. 12), primarily in the NE-SW and NW-SE directions. France benefits from directional smoothing in both flat and complex terrain, particularly between the Massif Central and the Alps, where an orthogonal organization of sites (NW-SE) relative to

[4] Note that in meteorology, winds are named for the direction they originate from. Thus, a westerly wind blows toward the east.

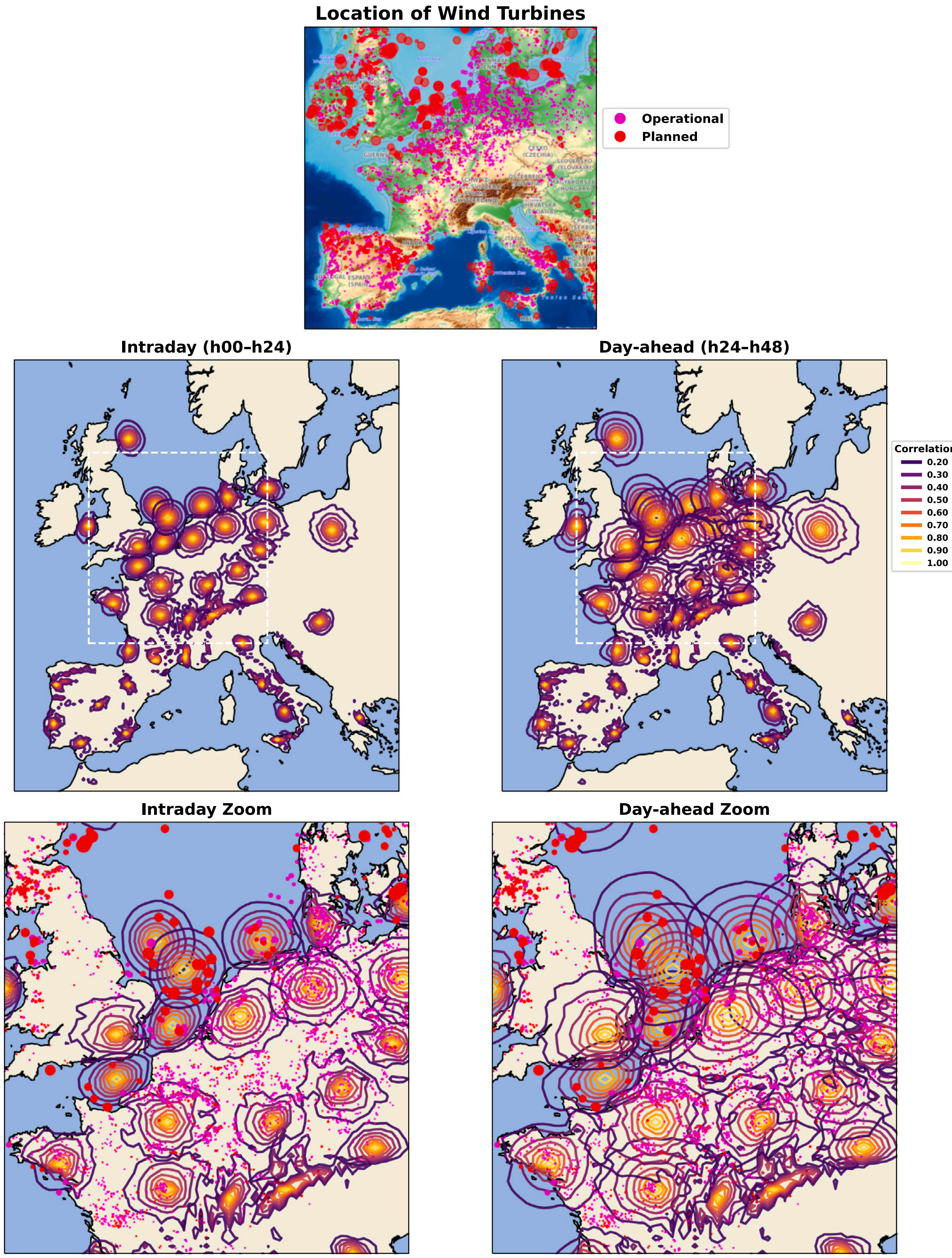

Fig. 13. Identification of correlated forecast error regions for wind energy. Upper plot: Black indicates existing wind turbines, red the planned wind turbines. The size of the dots relates to the capacity.

the main SE-FE direction (NE-SW) provides over 4% additional error smoothing potential.

In summary, exploiting the main FE directions benefits both solar and wind energy, with wind energy demonstrating a greater advantage (over 20% compared to around 5%).

3.4. Impact on the european energy portfolio

Finally, we derive implications for the European Energy portfolio by linking correlation maps to the installed and planned renewable energy capacities in Europe to identify centers of correlated FEs, we refer to as *FE hotspots*. The capacities for wind turbine sites are sourced from the *Global Wind Power Tracker* [30] and solar capacities from the *Global Solar Power Tracker* [31]. We focus on intraday and day-ahead lead times due to their significance in energy trading.

Spain is characterized by a diverse portfolio of wind turbines (Fig. 13) and PV capacities (Fig. 14), resulting in multiple FE hotspots with low inter-regional correlation. Given its vast land area and complex topography, Spain features distinct correlation hotspots, leading to a well-hedged, spatially-separated PV and wind energy portfolio. In *Portugal*, PV is concentrated in the south, while major operational and planned wind parks (onshore and offshore) are in the north, creating two distinct forecast error hotspots. *France* has a large land area and is geographically diverse, with regions in the European Plain and complex

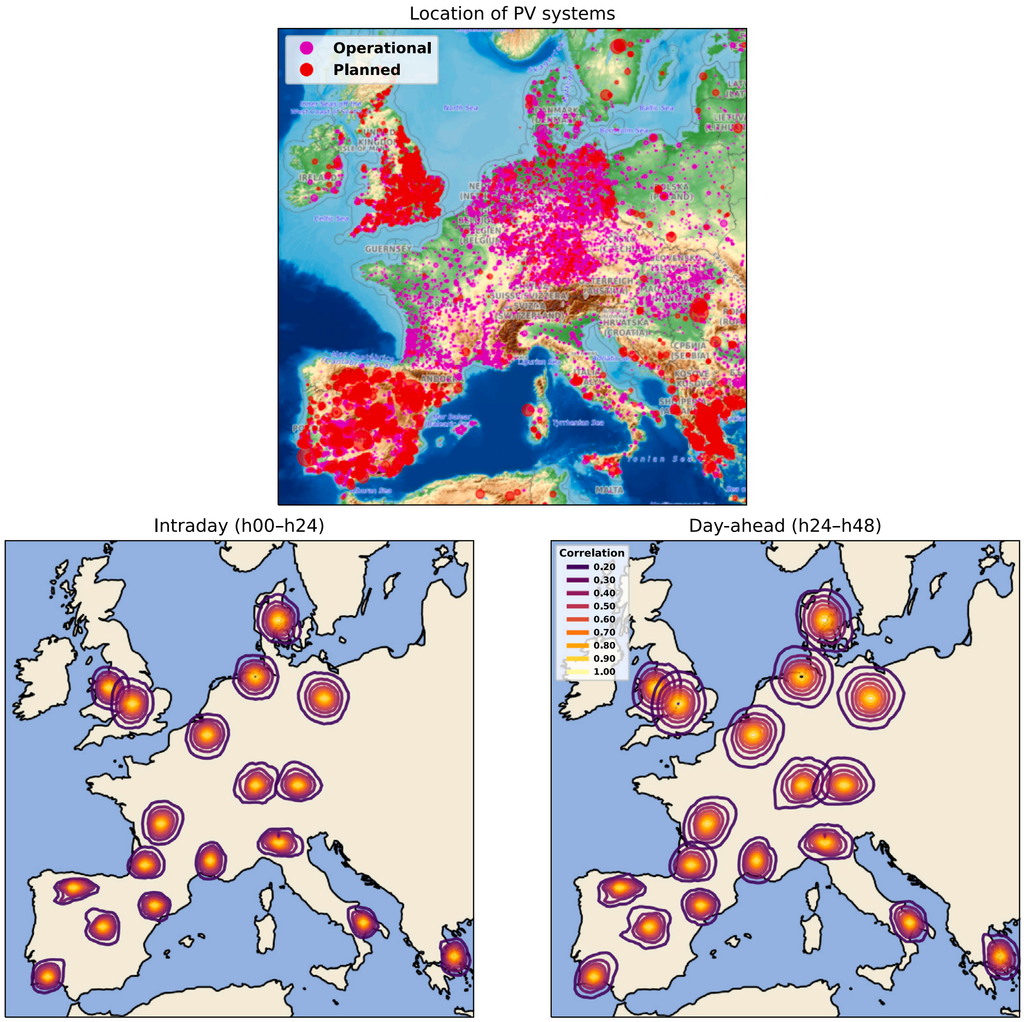

Fig. 14. Identification of correlated forecast error regions for wind energy forecast errors (Identical to Fig. 13, but for solar energy forecast errors and without a zoom-in.). Compared to wind, smaller error growths and more uniform correlation maps are noticeable.

terrains (Alps, Massif Central, Pyrenees). Strong correlations of SE-FEs are observed in the Rhone Valley and along the Garonne Valley, having both among the largest PV capacities in France, resulting in two SE-FE hotspots. Wind turbines are primarily situated along the western Atlantic coast and in northern France near Belgium, leading to two major WE-FE hotspots. The most critical region is in the *English Channel*, where extensive wind capacities are installed and planned. Adjacent to the UK, Belgium, and the Netherlands, this region has a high concentration of WE-FEs, while error growth from intraday to day-ahead severely magnifies the impacts. As Belgium and the Netherlands are small bidding zones, significant impacts across multiple countries can be anticipated in major markets, especially with planned wind expansions. SE-FEs (Fig. 14) have smaller error growth in this region, however, due to dense PV capacities in Belgium and the Netherlands, correlated country-level SE-FEs are expected. *Germany* shows a strong concentration of WE-FEs in the north and SE-FEs in the south and north-east, leading to three SE-FE hotspots (south-east, south-west, and north-east) and two WE-FE hotspots (North Sea and Baltic Sea). Due to its location in the European Plain, the WE-FE hotspots in Germany show significant growth in correlation maps from intraday to day-ahead lead times. Consequently, wind turbines in the North-West and North-East, which are independent at intraday lead times, can become dependent at day-ahead lead time. The Baltic and Northern Sea, with the largest offshore wind capacities, remain surprisingly independent at day-ahead lead times. Lastly, the *United Kingdom* and *Ireland* have a balanced portfolio of distributed offshore wind and PV capacities.

4. Discussion and limitations

4.1. Meteorological explanation of the results

As shown in this study, and in accordance with previous studies on WE-FEs [18,20], longer lead times are associated with larger spatial correlation scales of FEs. This can be attributed to error growth in NWP models: small-scale perturbations in the initial conditions of a chaotic atmospheric system can lead to diverging trajectories over time [32,33]. At lead times of 1–2 days, initially localized errors can grow upscale, project onto the synoptic-scale flow, amplify, and propagate downstream, thereby producing large-scale error structures [34,35]. This leads to low-frequency, spatially coherent errors and thus to longer correlation lengths [36,37]. The mid-latitudes are particularly prone to such error growth because of their strong baroclinicity [34].

WE-FEs are more strongly affected than SE-FEs, with a median increase in correlation length of about 25 km per day of lead time across all sites, whereas SE-FEs increase by only around 10 km per day. A plausible explanation is that wind forecasts depend strongly on large-scale atmospheric dynamics and that near-surface wind is additionally modulated by orography and land-surface roughness. By contrast, solar radiation is less directly affected by orography and is more strongly influenced by localized processes such as cloud evolution and fog. Consistent with this interpretation, WE-FEs already exhibit larger correlation lengths than SE-FEs at intraday lead times (more than 100 km versus around 50 km), but the increase with lead time is stronger for wind. Furthermore, we find a clear seasonal dependence of correlation lengths, particularly for WE-FEs: at a 2-day lead time, correlation lengths are about 60 km larger in winter than in summer. This seasonal contrast is also consistent with stronger baroclinic instability in winter than in summer, while Northern Europe is more prone to stronger baroclinic instability than Southern Europe visible in larger correlation lengths.

4.2. Importance of the results for decision-makers in the energy domain

This study provides decision makers in the energy sector with valuable information. FEs become uncorrelated at distances greater than 150 km, leading to noticeable smoothing effects. However, to achieve substantial smoothing, larger areas are necessary. At the day-ahead stage, FEs are largely reduced for areas of 200 × 200 km, decreasing MAE, variability, and the occurrence of extreme events by approximately one-third for WE-FEs and by around 25% for SE-FEs. Given these large error reductions, it is worth questioning whether site separation of new plants from the existing portfolio should be considered in decision-making. Today, investments rely on the critically important energy potential at a given site. This overlooks the portfolio risk from a renewable site with significant spatial dependencies. Increasing the distance between renewable energy sites can be a simple way to significantly reduce total expected forecast errors and smooth the errors in existing portfolios, thus lowering countertrading costs.

In the current European portfolio, several FE hotspots were identified. These include the WE-FEs in the English Channel affecting Belgium, the United Kingdom, and the Netherlands, which have a high concentration of planned offshore wind parks. Additionally, SE-FEs have been identified in South-East, South-West, and Eastern Germany. Smart hedging and control strategies are essential to mitigate strong errors in this region, such as those caused by electricity grid expansions, storage capacities, or hydrogen production.

Lastly, this study shows a strong increase in spatial dependence from intraday to day-ahead. Therefore, given the growth of errors from intraday to day-ahead range, increasing market volumes on markets with shorter lead times (intraday) can help mitigate large-scale forecast errors. For these time scales, significant advances in the renewable energy research community, beyond NWP models, provide accurate forecasts, such as lidar-based wind forecasts and camera- and satellite-based solar energy forecasts. Shifting market volumes from day-ahead to intraday markets can significantly reduce the criticality of FE hotspots. While this results in shorter reaction times for countermeasures, smaller imbalance volumes due to reduced spatial dependence and forecast errors would be necessary, which could potentially be managed by fast-response solutions like batteries.

4.3. Limitations and further research avenues

In this study, we focused on synoptic-scale FEs with coarse hourly forecasts (0.25°) from the operational ECMWF IFS model to ensure spatial and temporal completeness. Forecasts from NWP models are the primary source for renewable energy forecasts in the energy sector [1] and energy system models are mainly based on hourly weather data. However, higher spatio-temporal resolution forecasts are available such as the currently operational ECMWF IFS model (around 9 km)[5] or other regional NWP models (e.g. ICON-EU with 13 km or ICON-D2 with 2 km resolution). Furthermore, satellite-based [6,38] or all-sky camera-based solar irradiance nowcasts [4,39] and lidar-based wind forecasts [40] outperform NWP forecasts for intraday lead times. It remains open how the findings of this study translate to finer spatio-temporal domains relevant for decision-making at very short lead times, which is also meteorologically interesting, as cloud resolving models exhibit error growth rates up to 10 times larger due to greater reliance on convective instabilities than on baroclinic instabilities [33].

Another interesting research avenue is to further analyze the effect of weather situations on the spatial dependence and smoothing potential of FEs. The severity and direction of correlated forecast error structures are likely influenced by large-scale atmospheric flow. This hypothesis aligns with findings that the dominant weather regime significantly affects wind speed and direction, as well as solar radiation potential [41]. It is thus likely, that different weather situations described through indices (e.g. North Atlantic Oscillation), focused weather patterns [42] or weather regimes [41], influence the magnitude and the direction of the spatial dependence during these weather conditions. This not only enhances our understanding but also provides forecasters and decision makers with valuable information about large-scale FEs in weather situations, which often show reasonable forecast skill even at subseasonal to seasonal time scales [43].

Another assumption in this study is that the PV and wind portfolio contains one characteristic fixed PV panel and characteristic wind turbines for onshore and offshore. The existing European renewable energy portfolio includes various configurations of PV modules and wind turbines, which could enhance the heterogeneity of technical renewable sites and increase the diversity of renewable energy feed-ins. It has been illustrated that exploiting PV panel orientations can reduce solar energy intermittency [44] and incorporating diverse renewable energy configurations, along with the proposed spatial separation in this study, could further mitigate correlated FEs.

Lastly, we examined only FEs in this study and omitted the downstream decision-making problem. Future studies could integrate the forecast error time series from this study into decision-making processes, supporting renewable energy site planning and potentially enhancing the robustness of large-scale energy system models against forecast errors. This is particularly relevant because current energy system models overlook renewable energy forecasts, resulting in economically inadequate systems [45].

5. Conclusions

The spatial dependency of renewable energy FEs in Europe has received little attention, despite its relevance for operational decision-making in energy. We derived site-specific correlation lengths and principal directions of forecast errors, showing that FEs lose their spatial correlation beyond 150 km, while WE-FEs have up to 60 km longer correlation lengths in winter than in summer. In the European Plain, larger spatial dependencies and a stronger error growth with longer lead times create significant correlated WE-FE hotspots, particularly in the English Channel for current and planned offshore wind capacities. Spatial separation of renewable sites can achieve significant smoothing. Regions of approximately 200 × 200 km can reduce FEs by around 33% for wind energy and 25% for SE-FEs. The predominant error direction is from west to east, consistent with the westerlies in Europe. Leveraging principal directions can increase the smoothing effect up to 20% for the same region for wind energy and by around 5% for solar energy. These findings enhance the understanding of spatial characteristics of FEs in Europe and support the design and operation of FE-hedged portfolios relevant for portfolio managers, distribution grid operators, and energy system planners.

[5] This study uses the same model, but averages the output to match the ERA5 resolution.

CRediT authorship contribution statement

Matthias Zech: Writing – review & editing, Writing – original draft, Visualization, Validation, Supervision, Software, Resources, Project administration, Methodology, Investigation, Funding acquisition, Formal analysis, Data curation, Conceptualization. **Marion Schroedter-Homscheidt:** Writing – review & editing, Visualization, Validation, Supervision, Software, Resources, Project administration, Methodology, Investigation, Funding acquisition, Formal analysis, Data curation, Conceptualization. **Lueder von Bremen:** Writing – review & editing, Visualization, Validation, Supervision, Software, Resources, Project administration, Methodology, Investigation, Funding acquisition, Formal analysis, Data curation, Conceptualization.

Declaration of competing interest

The authors declare the following financial interests/personal relationships which may be considered as potential competing interests: Matthias Zech reports financial support was provided by German Federal Environmental Foundation. If there are other authors, they declare that they have no known competing financial interests or personal relationships that could have appeared to influence the work reported in this paper.

Acknowledgments

The work was carried out within the national research project "SOLREV" (FKZ 03EE1010E) funded by the Federal Ministry for Economic Affairs and Climate Action (BMWK) on the basis of a decision by the German Bundestag. M. Zech was supported by the German Federal Environmental Foundation within the PhD scholarship (grant no. 20020/667-33/2). Furthermore, we thank the Solrev partners and in particular Elke Lorenz for helpful comments that improved the quality of this paper.

Data availability

The data are available from the corresponding author upon request. Reanalysis data from ERA5 and satellite data can be downloaded by using the `atlite` library. The used forecasts can be downloaded from the Meteorological Archival and Retrieval System (MARS) at ECMWF for registered users.

References

[1] C. Sweeney, R.J. Bessa, J. Browell, P. Pinson, The future of forecasting for renewable energy, Wiley Interdiscip. Rev.: Energy Environ. 9 (2) (2020) http://dx.doi.org/10.1002/wene.365.

[2] Q. Paletta, G. Terrén-Serrano, Y. Nie, B. Li, J. Bieker, W. Zhang, L. Dubus, S. Dev, C. Feng, Advances in solar forecasting: Computer vision with deep learning, Adv. Appl. Energy 11 (August) (2023) 100150, http://dx.doi.org/10.1016/j.adapen.2023.100150.

[3] A. Ahmed, M. Khalid, A review on the selected applications of forecasting models in renewable power systems, Renew. Sustain. Energy Rev. 100 (March 2018) (2019) 9–21, http://dx.doi.org/10.1016/j.rser.2018.09.046.

[4] T. Schmidt, M. Calais, E. Roy, A. Burton, D. Heinemann, T. Kilper, C. Carter, Short-term solar forecasting based on sky images to enable higher PV generation in remote electricity networks, Renew. Energy Environ. Sustain. 2 (2017) 23, http://dx.doi.org/10.1051/rees/2017028.

[5] S.A. Logothetis, V. Salamalikis, S. Wilbert, J. Remund, L.F. Zarzalejo, Y. Xie, B. Nouri, E. Ntavelis, J. Nou, N. Hendrikx, L. Visser, M. Sengupta, M. Pó, R. Chauvin, S. Grieu, N. Blum, W. van Sark, A. Kazantzidis, Benchmarking of solar irradiance nowcast performance derived from all-sky imagers, Renew. Energy 199 (2022) 246–261, http://dx.doi.org/10.1016/j.renene.2022.08.127.

[6] A. Hammer, D. Heinemann, E. Lorenz, B. Lückehe, Short-term forecasting of solar radiation: A statistical approach using satellite data, Sol. Energy 67 (1–3) (1999) 139–150, http://dx.doi.org/10.1016/s0038-092x(00)00038-4.

[7] S.R. West, D. Rowe, S. Sayeef, A. Berry, Short-term irradiance forecasting using skycams: Motivation and development, Sol. Energy 110 (2014) 188–207, http://dx.doi.org/10.1016/j.solener.2014.08.038.

[8] L. Valldecabres, A. Penã, M. Courtney, L. Von Bremen, M. Kühn, Very short-term forecast of near-coastal flow using scanning lidars, Wind. Energy Sci. 3 (1) (2018) 313–327, http://dx.doi.org/10.5194/wes-3-313-2018.

[9] P. Bauer, A. Thorpe, G. Brunet, The quiet revolution of numerical weather prediction, Nature 525 (7567) (2015) 47–55, http://dx.doi.org/10.1038/nature14956.

[10] I. Price, A. Sanchez-Gonzalez, F. Alet, T.R. Andersson, A. El-Kadi, D. Masters, T. Ewalds, J. Stott, S. Mohamed, P. Battaglia, R. Lam, M. Willson, Probabilistic weather forecasting with machine learning, Nature (2024) http://dx.doi.org/10.1038/s41586-024-08252-9.

[11] O. Gandhi, W. Zhang, D.S. Kumar, C.D. Rodríguez-Gallegos, G.M. Yagli, D. Yang, T. Reindl, D. Srinivasan, The value of solar forecasts and the cost of their errors: A review, (ISSN: 18790690) 2024, http://dx.doi.org/10.1016/j.rser.2023.113915.

[12] R. Perez, S. Kivalov, J. Schlemmer, K. Hemker, T.E. Hoff, Short-term irradiance variability: Preliminary estimation of station pair correlation as a function of distance, (ISSN: 0038092X) 2012, http://dx.doi.org/10.1016/j.solener.2012.02.027.

[13] C.M. St. Martin, J.K. Lundquist, M.A. Handschy, Variability of interconnected wind plants: Correlation length and its dependence on variability time scale, Environ. Res. Lett. 10 (4) (2015) http://dx.doi.org/10.1088/1748-9326/10/4/044004.

[14] M. Sengupta, A. Habte, S. Wilbert, C. Gueymard, J. Remund, E. Lorenz, W. van Sark, A.R. Jensen, Best Practices Handbook for the Collection and Use of Solar Resource Data for Solar Energy Applications: Fourth Edition, Technical Report, IEA PVPS Task 16, 2024.

[15] E. Lorenz, J. Hurka, D. Heinemann, H.G. Beyer, Irradiance forecasting for the power prediction of grid-connected photovoltaic systems, IEEE J. Sel. Top. Appl. Earth Obs. Remote. Sens. 2 (1) (2009) 2–10, http://dx.doi.org/10.1109/JSTARS.2009.2020300.

[16] R. Perez, M. David, T.E. Hoff, M. Jamaly, S. Kivalov, J. Kleissl, P. Lauret, M. Perez, Spatial and temporal variability of solar energy, Found. Trends® Renew. Energy 1 (1) (2016) 1–44, http://dx.doi.org/10.1561/2700000006.

[17] N. Saleck, L. Von Bremen, Wind power forecast error smoothing within a wind farm, J. Phys.: Conf. Ser. 75 (1) (2007) http://dx.doi.org/10.1088/1742-6596/75/1/012051.

[18] U. Focken, M. Lange, K. Mönnich, H. Waldl, H. Beyer, A. Luig, A statistical analysis of the reduction of the wind power prediction error by spatial smoothing effects, J. Wind Eng. Ind. Aerodyn. 90 (July 2001) (2002) 231–246.

[19] J.J. Miettinen, H. Holttinen, Characteristics of day-ahead wind power forecast errors in Nordic countries and benefits of aggregation, Wind. Energy 20 (6) (2017) 959–972, http://dx.doi.org/10.1002/we.2073.

[20] M. Hüsch, B.U. Schyska, L. von Bremen, CorClustST—Correlation-based clustering of big spatio-temporal datasets, Future Gener. Comput. Syst. 110 (2020) 610–619, http://dx.doi.org/10.1016/j.future.2018.04.002.

[21] D. Schönheit, M. Kenis, L. Lorenz, D. Möst, E. Delarue, K. Bruninx, Toward a fundamental understanding of flow-based market coupling for cross-border electricity trading, Adv. Appl. Energy 2 (April) (2021) http://dx.doi.org/10.1016/j.adapen.2021.100027.

[22] H. Hersbach, B. Bell, P. Berrisford, S. Hirahara, A. Horányi, J. Muñoz-Sabater, J. Nicolas, C. Peubey, R. Radu, D. Schepers, A. Simmons, C. Soci, S. Abdalla, X. Abellan, G. Balsamo, P. Bechtold, G. Biavati, J. Bidlot, M. Bonavita, G. De Chiara, P. Dahlgren, D. Dee, M. Diamantakis, R. Dragani, J. Flemming, R. Forbes, M. Fuentes, A. Geer, L. Haimberger, S. Healy, R.J. Hogan, E. Hólm, M. Janisková, S. Keeley, P. Laloyaux, P. Lopez, C. Lupu, G. Radnoti, P. de Rosnay, I. Rozum, F. Vamborg, S. Villaume, J.N. Thépaut, The ERA5 global reanalysis, Q. J. R. Meteorol. Soc. 146 (730) (2020) 1999–2049, http://dx.doi.org/10.1002/qj.3803.

[23] U. Pfeifroth, J. Drücke, S. Kothe, J. Trentmann, M. Schröder, R. Hollmann, SARAH-3 – satellite-based climate data records of surface solar radiation, Earth Syst. Sci. Data 16 (11) (2024) 1–28, http://dx.doi.org/10.5194/essd-16-5243-2024.

[24] D. Yang, J.M. Bright, Worldwide validation of 8 satellite-derived and reanalysis solar radiation products: A preliminary evaluation and overall metrics for hourly data over 27 years, Sol. Energy 210 (November 2019) (2020) 3–19, http://dx.doi.org/10.1016/j.solener.2020.04.016.

[25] M. Zech, A. Hammer, J. Trentmann, U. Pfeifroth, Harmonizing the hourly solar radiation calculation from satellite-derived irradiance, Sol. Energy 305 (305) (2026) 114243, http://dx.doi.org/10.1016/j.solener.2025.114243.

[26] F. Hofmann, J. Hampp, F. Neumann, T. Brown, J. Hörsch, atlite: A Lightweight Python Package for Calculating Renewable Power Potentials and Time Series, J. Open Source Softw. 6 (62) (2021) 3294, http://dx.doi.org/10.21105/joss.03294.

[27] J. Hörsch, F. Hofmann, D. Schlachtberger, T. Brown, PyPSA-Eur: An open optimisation model of the European transmission system, Energy Strat. Rev. 22 (August) (2018) 207–215, http://dx.doi.org/10.1016/j.esr.2018.08.012.

[28] T. Hastie, R. Tibshirani, J. Friedman, The elements of statistical learning: data mining, inference, and prediction, in: Elements of Statistical Learning, second ed., Springer New York, NY, New York, 2009, p. 745, http://dx.doi.org/10.1007/978-0-387-84858-7.

[29] J.R. Holton, G.J. Hakim, An introduction to dynamic meteorology: Fifth edition, in: An Introduction To Dynamic Meteorology: Fifth Edition, vol. 9780123848, 2012, pp. 1–532, http://dx.doi.org/10.1016/C2009-0-63394-8.

[30] Global Energy Monitor, Global Energy Monitor - Global Wind Power Tracker, 2022.

[31] Global Energy Monitor, Global Energy Monitor - Global Solar Power Tracker, 2023.

[32] E.N. Lorenz, The predictability of a flow which possesses many scales of motion, Tellus A: Dyn. Meteorol. Ocean. 21 (3) (1969) 289, http://dx.doi.org/10.3402/tellusa.v21i3.10086.

[33] C. Hohenegger, C. Schär, Atmospheric predictability at synoptic versus cloud-resolving scales, Bull. Am. Meteorol. Soc. 88 (11) (2007) 1783–1793, http://dx.doi.org/10.1175/BAMS-88-11-1783.

[34] M. Baumgart, M. Riemer, V. Wirth, F. Teubler, S.T. Lang, Potential vorticity dynamics of Forecast errors: A quantitative case study, Mon. Weather Rev. 146 (5) (2018) 1405–1425, http://dx.doi.org/10.1175/MWR-D-17-0196.1.

[35] H.C. Davies, M. Didone, Diagnosis and dynamics of forecast error growth, Mon. Weather Rev. 141 (7) (2013) 2483–2501, http://dx.doi.org/10.1175/MWR-D-12-00242.1.

[36] J. Oswald, M. Raine, H. Ashraf-Ball, Will British weather provide reliable electricity? Energy Policy 36 (8) (2008) 3212–3225, http://dx.doi.org/10.1016/j.enpol.2008.04.033.

[37] J. Huang, X. Lu, M.B. McElroy, Meteorologically defined limits to reduction in the variability of outputs from a coupled wind farm system in the Central US, Renew. Energy 62 (2014) 331–340, http://dx.doi.org/10.1016/j.renene.2013.07.022.

[38] A. Roy, A. Hammer, D. Heinemann, O. Lünsdorf, J. Lezaca, Impact of tropical convective conditions on solar irradiance forecasting based on cloud motion vectors, Environ. Res. Lett. 17 (10) (2022) http://dx.doi.org/10.1088/1748-9326/ac94e6.

[39] N.B. Blum, Nowcasting of Solar Irradiance and Photovoltaic Production Using a Network of All-Sky Imagers Analyse und Vorhersage von Solarstrahlung und PV-Erzeugung mittels eines Wolkenkamera-Netzwerks, Technical Report, RWTH Aachen University, Aachen, 2022.

[40] F. Theuer, M.F. van Dooren, L. von Bremen, M. Kühn, Lidar-based minute-scale offshore wind speed forecasts analysed under different atmospheric conditions, Meteorol. Z. 31 (1) (2022) 13–29, http://dx.doi.org/10.1127/metz/2021/1080.

[41] C.M. Grams, R. Beerli, S. Pfenninger, I. Staffell, H. Wernli, Balancing Europe's wind-power output through spatial deployment informed by weather regimes, Nat. Clim. Chang. 7 (8) (2017) 557–562, http://dx.doi.org/10.1038/NCLIMATE3338.

[42] M. Zech, L. von Bremen, Improving Short-Term, Near-Surface Temperature Forecasts by Integrating Weather Pattern Information into Model Output Statistics, Mon. Weather Rev. 152 (8) (2024) 1711–1723, http://dx.doi.org/10.1175/mwr-d-23-0134.1.

[43] D. Büeler, L. Ferranti, L. Magnusson, J.F. Quinting, C.M. Grams, Year-round sub-seasonal forecast skill for Atlantic–European weather regimes, Q. J. R. Meteorol. Soc. 147 (741) (2021) 4283–4309, http://dx.doi.org/10.1002/qj.4178.

[44] M. Zech, L. von Bremen, Data-driven mean-variability optimization of PV portfolios with automatic differentiation, in: ICLR 2023 Workshop: Tackling Climate Change with Machine Learning, Kigali, 2023.

[45] F. Peterssen, M. Schlemminger, C. Lohr, R. Niepelt, R. Hanke-Rauschenbach, R. Brendel, Impact of forecasting on energy system optimization, Adv. Appl. Energy 15 (2024) http://dx.doi.org/10.1016/j.adapen.2024.100181.